Research Square

Preprints are preliminary reports that have not undergone peer review.
They should not be considered conclusive, used to inform clinical practice,
or referenced by the media as validated information.

Machine Learning–Driven Inverse Design of Gradient Porous Elastomers for High-Performance Flexible Pressure Sensors

Yingle Xue
Beijing Institute of Technology
Jiaxing He
Sun Yat-sen University
Jingfa Li
Yangtze University
Ningning Song
Beijing Institute of Technology
Sijie Yin
Beijing Institute of Technology
Minmin Liang
mmliang@bit.edu.cn

Beijing Institute of Technology

Article

Keywords:

Posted Date: November 11th, 2026

DOI: https://doi.org/10.21203/rs.3.rs-11186204/v1

License: This work is licensed under a Creative Commons Attribution 4.0 International License.
Read Full License

Additional Declarations: No competing interests reported.

Machine Learning–Driven Inverse Design of Gradient Porous Elastomers for High-Performance Flexible Pressure Sensors

Yingle Xue [a], Jiaxing He [b], Jingfa Li [c], Ningning Song [d], Sijie Yin [a]*, Minmin Liang [d]**

a School of Automation, Beijing Institute of Technology, Beijing, 100081, China

b School of Systems Science and Engineering, Sun Yat-sen University, Guangzhou 510275, China

c School of Petroleum Engineering, Yangtze University, 430100, China

d Experimental Center of Advanced Materials, School of Materials Science and Engineering, Beijing Institute of Technology, Beijing, 100081, China

* Correspondence: songningning@bit.edu.cn; yinsijie@bit.edu.cn; mmliang@bit.edu.cn

Abstract

Introducing gradient porous microstructures offers a cost-effective and easily scalable approach for developing flexible thin-film pressure sensors. However, the vast design space arising from varying pore sizes and combinations renders the identification of optimal structural parameter nearly unattainable through conventional trial-and-error experiments. Herein, we propose a novel methodology that integrates finite element simulation with machine learning to efficiently search for the optimal solution. A finite element model of the gradient porous dielectric layer is established using COMSOL, incorporating an equivalent parameter inversion strategy. Hundreds of pressures–capacitance response datasets are generated through parametric simulations and subsequently employed to train a backpropagation (BP) neural network surrogate model. The optimized structural parameters are then experimentally validated through the fabrication of a thin-film pressure sensor. The fabricated sensor exhibits fast response and recovery time (75 ms), a low detection limit (0.2 kPa), a wide detection

range (600 kPa), and outstanding long-term stability over 5,000 cycles. Furthermore, the sensor demonstrates excellent applicability in various scenarios, including human physiological signal monitoring and speech recognition. More importantly, the integrated simulation–machine learning framework presented herein is broadly applicable to other structural designs, offering a powerful alternative to traditional trial-and-error approaches and substantially reducing development costs.

Introduction

Flexible thin-film pressure sensors are widely used in consumer electronics, industrial automation, and health monitoring [1–4]. Despite the substantial number of sensors reported in the past decades, most studies have followed one of two technical approaches. The first approach relies on chemically synthesized composite materials, in which the skeletal network of cellulose [5-6], polyurethane [7-8], or polydimethylsiloxane [9-10] are chemically modified to enable molecular-scale elastic deformation, while conductive fillers such as graphene [11–13], carbon black [14–16], carbon nanotubes [17–19], and MXene [20–22] are incorporated to construct efficient conductive networks. Pressure-induced variations in interlayer spacing at the molecular level result in changes in electrical signals. Although this strategy has achieved promising performance in terms of sensitivity and sensing range, it is often limited by complex fabrication processes, long production cycles, poor sample uniformity, and low yield, which collectively limit its practical application.

The second approach focuses on structural design at the physical level. Researchers have utilized elastomers such as PDMS [23-25] and Ecoflex [26-28] to fabricate various microstructures, including pyramidal [29-30], hemispherical [31-32], and microcolumn/microneedle [33-34] through advanced manufacturing techniques. These structures improve sensor performance by tuning deformation behavior and contact area changes under applied pressure. Although this approach avoids the complexities of chemical reactions and the instabilities involved in the synthesis of composite materials, thereby improving sample uniformity and yield, the fabrication processes are

still relatively complex and costly, which limits large-scale production. To the best of our knowledge, flexible thin-film pressure sensors have not yet achieved a balance across multiple performance metrics, including cost control, flexibility, measurement range, and sensitivity.

The introduction of gradient porous microstructures [35–36] into thin-film pressure sensors provides an available strategy for improving the comprehensive performance mentioned above, owing to its easier fabrication process, scalable potential and low-cost. However, the large number of possible combinations of pore sizes and layer numbers makes it difficult to quickly identify optimal structural parameters. Previously reported design methods usually rely on simplified analytical models and trial-and-error experiments to tune microstructures for target performance [37–38], which becomes highly time-consuming in high-dimensional design spaces. Moreover, the complex and highly nonlinear relationships among material properties, structural parameters, and sensor performance further increase the difficulty of optimization. Machine learning models can effectively capture these nonlinear relationships between material properties, structural parameters, and sensor responses [39–40], enabling rapid prediction of optimal structural combinations without the need for extensive repeated experiments.

Accordingly, this manuscript proposes a novel methodology for the cost-effective design of flexible pressure-sensing thin films by integrating machine learning with simulation techniques (**Fig. 1**). An ultrathin capacitive pressure sensor featuring a three-layer gradient porous structure (TGPS) is first fabricated as an experimental sample. Based on the pore size and pressure–capacitance response of the experimental samples, the material model is calibrated using COMSOL simulations to identify the nonlinear relationship between pore structure parameters and material behavior, establishing a parameterized modeling and batch solution workflow **(Fig. 1a)**. A large-scale dataset containing pore sizes and pressure-capacitance responses is generated using Latin hypercube sampling **(Fig. 1b)**, and a backpropagation (BP) neural network is trained as a surrogate model to explore the parameter space and identify optimal structural parameters **(Fig. 1c)**. This approach effectively overcomes the limitations of traditional

trial-and-error methods, including low efficiency and insufficient exploration of the design space. Following rational design and optimization, the proposed sensor can accurately monitor arterial pulse waves and detect speech through throat muscle movements (**Fig. 1d)**. By integrating the sensor with a convolutional neural network, a high-accuracy speech recognition system is developed, achieving 98.89% accuracy in a 20-word classification task (**Fig. 1e).** These results not only demonstrate the excellent performance of the sensor but also highlights its broad application potential in intelligent speech interaction and health monitoring, providing new design insights for next-generation flexible sensing systems in wearable applications.

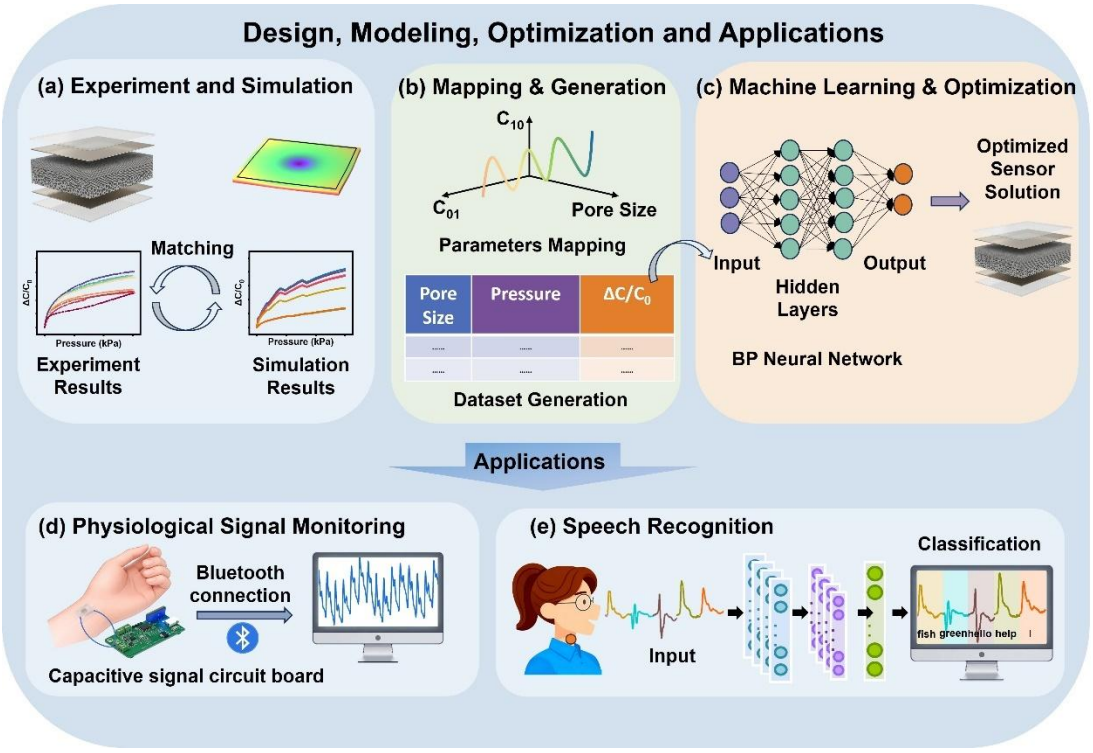


Fig. 1 Overview of sensor design, optimization and applications. **a** Experiment samples and simulation modeling of sensors. **b** Sensor parameter mapping and dataset construction. c Prediction of optimal sensor structure using machine learning. **d-e** Human physiological signals monitoring and speech recognition using the proposed sensor.

Results and Discussion

Optimization of structural parameters

The pore size significantly influences on the sensitivity of multi-layer gradient porous pressure sensors. In previous literatures, pore size selection predominantly relied on researchers' experimental experience and theoretical simulations. However, the inherent complexity of porous structures complicates theoretical modeling, while variability in individual experiences may lead to the omission of optimal parameters. To address this challeng, this work proposes a global parameter optimization method combining finite element simulation and machine learning (**Fig. 2a)**.

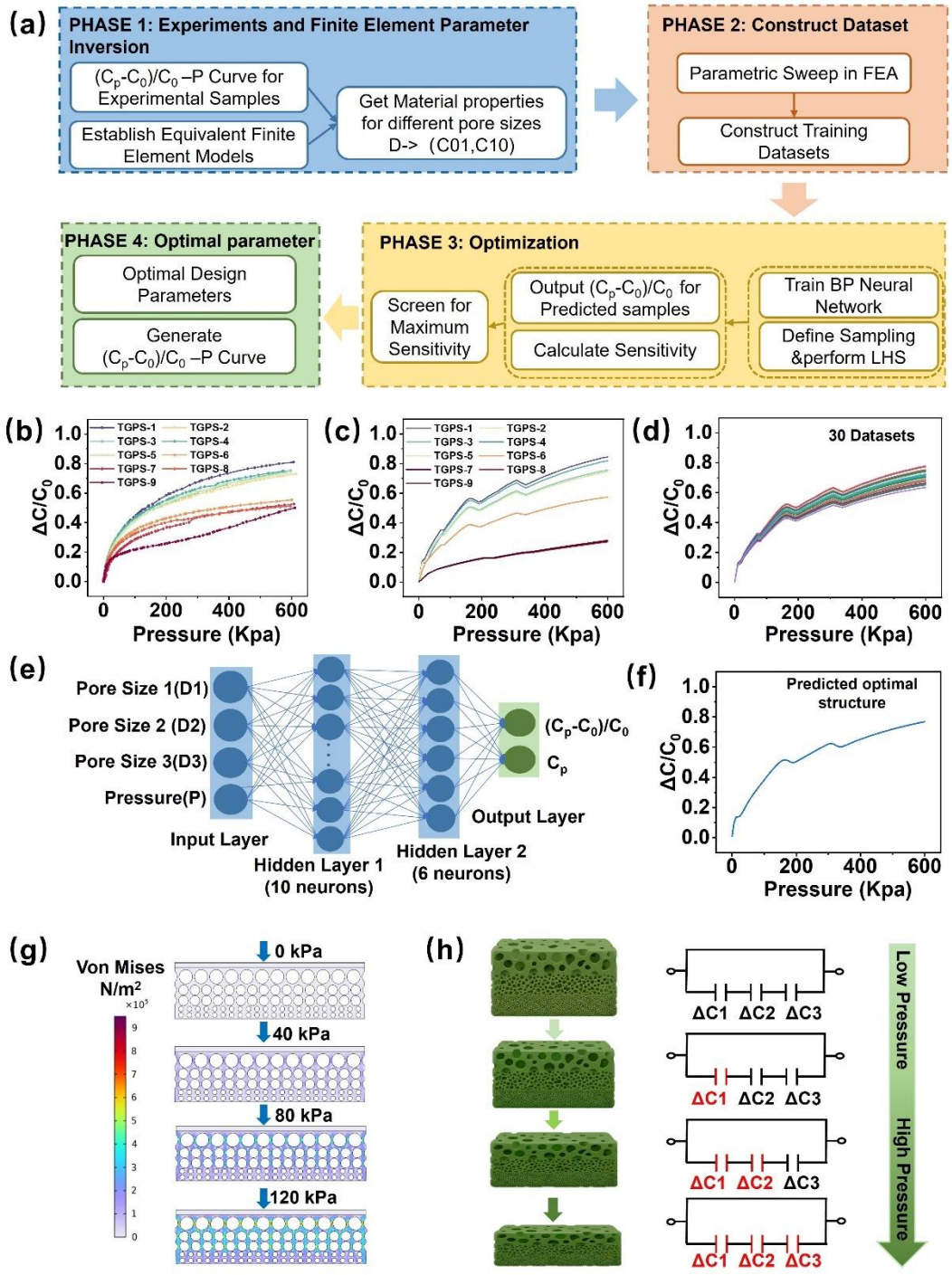


Fig. 2 Overview of the experimental, modeling, optimization process. **a** Flowchart of the process combining simulation and machine learning. **b** Pressure-capacitance response of the experimental sample. **c** Pressure-capacitance response of the simulated sample. **d** Pressure-capacitance response of a portion of the dataset. **e** Schematic diagram of the BP neural network algorithm. **f** Pressure-capacitance response of the

theoretically optimal structure. **g** Compressive deformation mechanism of a gradient porous pressure sensor based on finite element simulation analysis. h Schematic diagram illustrating the operating principle of the gradient porous pressure sensor under varying applied pressures.

The proposed global parameter optimization method comprises four sequential phases (Fig. 2a).

Phase 1: Experimental sample preparation and finite element inversion. Nine sets of experimental samples with varying pore size (**Table S1**), labeled TGPS-1 to TGPS-9, were first prepared using a sacrificial template method. Their capacity responses were measured over a pressure range of 0-600 kPa (**Fig. 2b**). The material model was then calibrated using finite element simulation (COMSOL Multiphysics) to ensure that the simulated capacitance behavior matched the experimental results (see Supporting Project Documents 1 for the nine simulation models). However, fully resolving the actual three-layer gradient porous film, which contains a large number of randomly distributed micron-scale pores, would require an extremely large finite element mesh and the strong coupling between large deformation of the hypereplastic material and the electrostatic field can easily lead to numerical divergence. Furthermore, only nine experimental samples were available for model calibration, precluding pore-by-pore reconstruction or repeated iterative simulations. To address these challenges, this study adopts a "macroscopic response-based equivalent parameter inversion" strategy, wherein each porous layer is treated as a homogeneous equivalent medium whose macroscopic mechanical and dielectric behaviors are described by equivalent hyperelastic parameters and an effective relative permittivity. This approach avoids the computational cost and convergence issues associated with explicit micro-pore modeling. Taking TGPS-1 as an example, its experimentally measured sensitivity curve was used as the target response. In COMSOL, the material parameters C_{10} and C_{01} in the Mooney–Rivlin constitutive model were defined as input variables. With the minimization of the sum of squared differences between the simulated and experimental curves as the optimization objective, the optimal equivalent material parameters for this

set of pore sizes set were obtained, enabling accurate reproduction of the macroscopic force–electrical response of TGPS-1 in simulation. By repeating this inversion process for TGPS2 through TGPS9, we established nine deterministic mappings of (D_1, D_2, D_3) → (C_{10}, C_{01}). This provides a foundation for parameter assignment and large-scale data generation for arbitrary pore size combination. **Fig. 2c** shows the pressure–capacitance responses of the nine simulation models.

Phase 2: Dataset construction. Latin hypercube sampling (LHS) was applied to the pore-size parameters and applied pressure, and batch calculations were performed to generate a large-scale dataset (300 sets, **Supporting Project Documents 2**) containing initial capacitance C_0, compressed capacitance C_p, and pressure-capacitance variations. Based on the established deterministic mapping (D_1, D_2, D_3) → (C_{10}, C_{01}) obtained from the nine experimental calibrations, equivalent material parameters can be assigned to arbitrary pore-size combinations, enabling fully controllable parametric simulations.

In this study, an automated parameter sweep and data extraction workflow was developed in COMSOL. The pore size ranges were defined as follows: D_1=160–200 μm, D_2=120–160 μm, and D_3=70–120 μm. Within these ranges, 300 random porous structural configurations were generated by randomly combining D_1, D_2, and D_3. For each configuration, the corresponding C_{10} and C_{01} values were obtained through mapping, and the material properties were automatically updated, along with the pore sizes of the three layers. In the equivalent model, the thickness of each layer was kept constant at 0.17 mm. Since the physical field was applied to a pore-free continuous medium, the pore size parameters were indirectly reflected only through the mapped material properties. Two study steps were implemented. First, a nonlinear solid mechanics analysis under pressure loading was performed to obtain the deformed configuration. Second, based on the deformed geometry, an electrostatic analysis was carried out to calculate the capacitance under pressure (C_p). In the zero-pressure state, a separate electrostatic simulation was performed to obtain the initial capacitance (C_0). The capacitance change under different pressures was then extracted to generate the

pressure–capacitance response curves. **Fig. 2d** shows the relative capacitance variation for 30 representative simulation samples. After completing all 300 simulation cases, the full dataset was exported, comprising the following input variables: D_1, D_2, D_3, and pressure P, and output variables: $\frac{Cp-C0}{C0}$ and C_p. This dataset served as the training and validation basis for the subsequent BP neural network surrogate model.

Phase 3: Optimization process. Using the 300 sets of generated simulation datasets as training samples, we established a rapid mapping from design parameters to performance metrics by constructing a BP neural network surrogate model, and performed global optimization and parameter sensitivity analysis on this surrogate model (**Supporting Project Documents 3**). The input variables were defined as a four-dimensional vector [D_1, D_2, D_3, P], and the output variables as a two-dimensional vector [$\frac{Cp-C0}{C0}$, C_p]. To improve the generalization ability of the neural network across the parameter space, we first used LHS to independently generate 20,000 uniformly distributed sample points within the ranges of the four input variables, forming a candidate set for prediction. To avoid the influence of scale differences between variables during training, a min–max normalization method was used to map each column of the input matrix into the range [−1, 1]. The original simulation dataset was used as the effective training set, while the 20,000 LHS samples were used solely for prediction and were not involved in training. A feedforward backpropagation neural network with a structure of 4–10–6–2, conprising two hidden layers with 10 and 6 neurons, respectively, was established (**Fig. 2e**). The training function employed the Bayesian regularization algorithm, with a maximum of 800 iterations. Within the network, all training samples were used for learning through the default data division function, and the built-in regularization mechanism was employed to reduce the risk of overfitting. After training, the normalized inputs of the 20,000 LHS samples were fed into the network to obtain normalized predictions, which were then denormalized back to physical values of $\frac{Cp-C0}{C0}$ and C_p. Based on the output, the sensitivity S was calculated

using the equation $S=\frac{Cp-C0}{C0\cdot P}$. From the 20,000 predicted results, the combination with the highest sensitivity was selected as the global optimal design parameter according to application requirements.

Phase 4: Determination of optimized parameters. By directly maximizing S, the surrogate-based global search identified the theoretical optimal structural parameters of the sensor as: pore size 1 (D_1) = 170.5μm, pore size 2 (D_2) = 133.9 μm, and pore size 3 (D_3) = 80.4 μm. **Fig. 2f** shows the pressure–capacitance response of this theoretically optimized structure. This approach avoids being trapped in local optima that may arise from sparse simulation data, and the surrogate model enables extremely fast prediction, allowing real-time evaluation of the design space.

To verify the reliability of the machine learning-assisted optimization results, 15 candidate structures (including the predicted optimal solution) were randomly selected from those predicted by the BP surrogate model and re-evaluated using the original COMSOL finite element model. The corresponding pressure–capacitance response curves were obtained and compared with the predictions of the BP surrogate model. The predicted and simulated results are summarized in **Table S2**. The COMSOL simulation results were treated as the ground truth, and the mean absolute percentage error (MAPE) was calculated to evaluate the prediction accuracy of the model. The average relative error of the model was only 2.96%, indicating a very high degree of consistency between the neural network predictions and the finite element simulation results. The established model can accurately predict the pressure-capacitance response of gradient porous structures under different parameter combinations, and the proposed simulation-machine learning integrated optimization method can reliably achieve global optimization of gradient porous structure parameters.

Sensing Performance of Gradient Porous Pressure Sensors

To reveal the synergistic regulation mechanism of pore size on the sensitivity of capacitive flexible pressure sensors, a comparative analysis of the experimental

samples (**Fig. 2b**) was conducted. The sensitivity of TGPS-6 is higher than that of TGPS-7 and TGPS-8. This is mainly because the elastic modulus of larger pores is lower, which makes the structure easier to deform under pressure and leads to larger capacitance changes. In contrast, structures with smaller pores exhibit a higher compressive modulus and limited deformation capability, resulting in reduced sensitivity. Notably, gradient structures generally demonstrate higher sensitivity compared to uniform porous architectures. This observation suggests that a single uniform structure cannot simultaneously achieve both high sensitivity and a wide sensing range. Instead, the coordinated deformation of multi-layer pore structures enables better overall performance. Furthermore, as the air gaps within the porous dielectric layer are progressively compressed, the effective dielectric constant changes accordingly. This coupling effect further enhances the sensitivity of the sensor within the same pressure range, outperforming traditional non-compressible porous structures.

Fig. 2g simulates the deformation behavior of the gradient porous pressure sensor. Owing to the low Young's modulus of the large-pore layer, deformation initiates in the top layer. As the pressure increases, the composite middle/small-pore layer and the remaining large-pore regions begin to deform successively. **Fig. 2h** models the gradient porous structure as an equivalent series connection of three capacitors. During the low-pressure phase, the top layer (C_1), characterized by large pores and low stiffness, deforms first, and the resulting capacitance change (ΔC_1) dominates the initial high sensitivity response. As pressure continues to increase, the top layer gradually approaches saturation, while the middle (C_2) and bottom (C_3) layers with more rigid structures sequentially begin to deform, generating ΔC_2 and ΔC_3 responses. This coupling effect effectively overcomes the common limitation of conventional uniform pore sensors, which tend to saturate under high pressure and thus exhibi a limited working range. Consequently, the gradient porous sensor maintains high sensitivity while achieving a significantly extended sensing range.

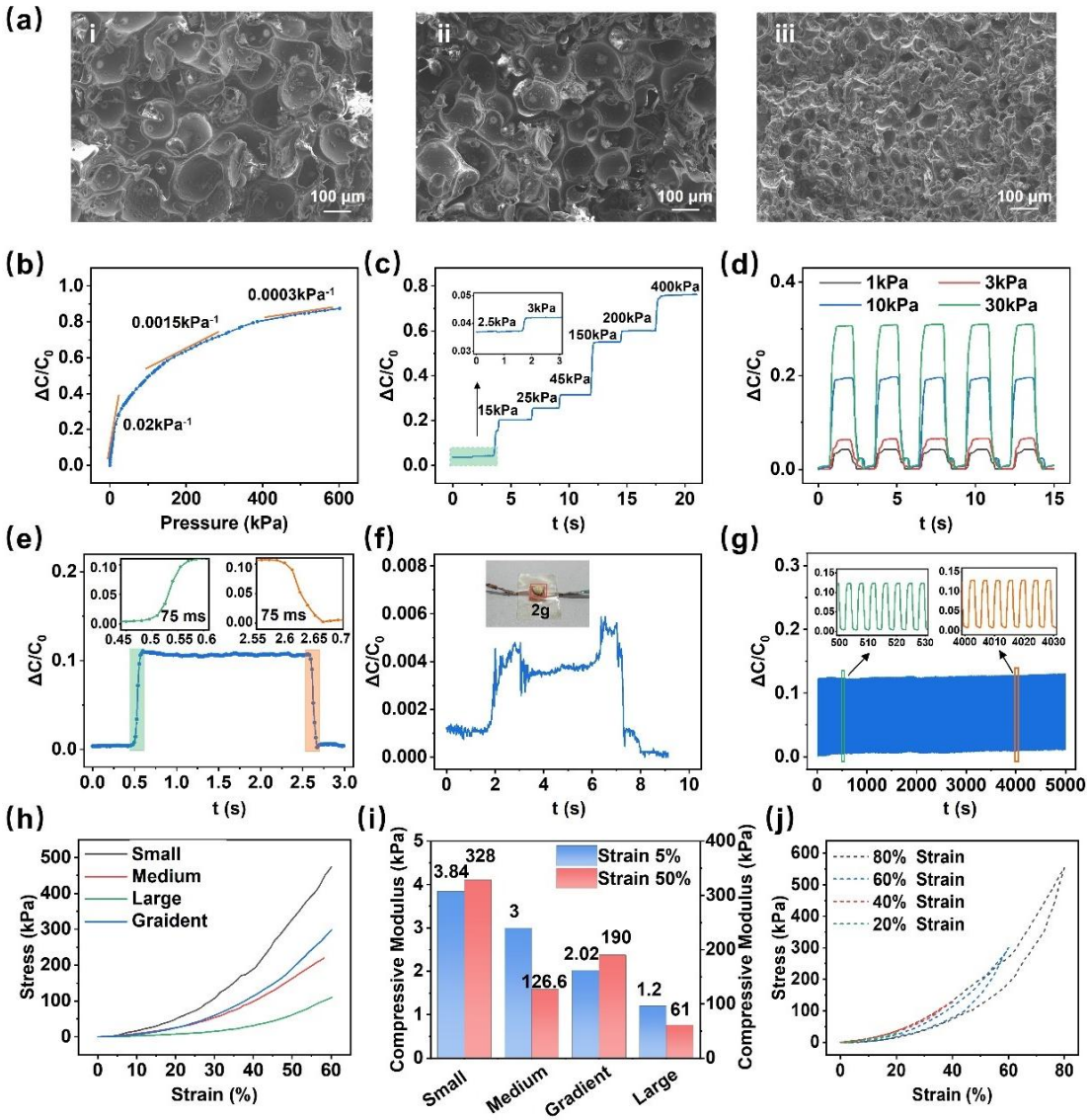


Fig. 3 Characterization and performance of the gradient porous capacitive pressure sensor. **a** SEM images of the porous layers, showing PMMA particle sizes of approximately 170.5 μm (i), 133.9 μm (ii), and 80.4 μm (iii), respectively. **b** Pressure-capacitance response of the sensor over a pressure range of 0-600 kPa. **c** Capacitive response of the sensor under stepwise pressure loading. **d** Normalized capacitance response at applied pressures of 1, 3, 10, and 30 kPa. **e** Response and recovery times of the pressure sensor at 10 kPa. **f** Relative capacitance changes at 0.2 kPa (2g load). **g** Long-term stability of the sensor over 5,000 loading/unloading cycles at 10 kPa. **h** Compressive stress-strain curves of sensors with gradient, small-pore, medium-pore, and large-pore structures. **i** Compressive modulus of sensors with gradient, small-pore,

medium-pore, and large-pore structures at different strain levels. **j** Hysteresis characteristics of the sensors at different strains.

Based on the theoretical optimal design parameters, which are 170.5 μm, 133.9 μm, and 80.4 μm for the three pore sizes, respectively, we fabricated the TPGS using a sacrificial template method. To obtain the desired particle size, the PMMA particles were ground in a mixture machine and then sieved to isolate fractions matching the theoretical optimized dimensions. **Fig. 3a** shows SEM images of the porous structures in each layer. Statistical analysis of the pore size distributions (**Fig. S7**) revealed that, for the large-pore layer, the pore diameters were mainly distributed within the range of 110–230 μm, with the highest frequency located around 170 μm, closely matching the machine-learning-predicted optimum of 170.52 μm. Similar distribution trends were observed for the medium- and small-pore layers, where the dominant pore sizes were concentrated near the optimized values of 133.88 and 80.43 μm, respectively. Although slight deviations between the experimental pore sizes and the designed parameters are inevitable due to inherent variability of the sacrificial template fabrication process, the majority of pores were distributed around the predicted optimal values, confirming good agreement between the fabricated gradient porous structures and the machine-learning-assisted design.

Fig. 3b shows the sensitivity of the TGPS over a pressure range of 0 to 600 kPa. The sensor exhibits a sensitivity of 0.02 kPa^{-1} in the 0–20 kPa range, 0.0015 kPa^{-1} in the 20–300 kPa range, and 0.0003 kPa^{-1} in the 300–600 kPa range. As shown in **Fig. 3c**, the sensor can clearly distinguish very small pressure differences, such as 2.5 kPa and 3 kPa, corresponding to a capacitance change equivalent to approximately 0.5 kPa. In addition, the sensor can distinctly detect stepwise pressure increments of 15, 25, 45, 150, 200, and 400 kPa through corresponding capacitance variations. To investigate the dynamic response characteristics, relative capacitance changes were characterized through five loading/unloading cycles at applied pressures of 1, 3, 10, and 30 kPa. The results show stable and reversible responses across all tested pressures (**Fig. 3d**).

Furthermore, **Fig. 3e** reveals that the sensor exhibits a short response and recovery time of 75ms under a 10 kPa stimulus, confirming its excellent dynamic performance. The detection limit is a critical parameter for evaluating the ability to sense small pressure signals. As shown in **Fig. 3f**, the sensor can clearly detect a very small pressure input of 0.2kPa, demonstrating a low detection limit. Sensor stability was further investigated by subjecting it to 5,000 loading/unloading cycles at 10 kPa. No obvious drift or performance degradation was observed (**Fig. 3g**), indicating excellent durability and long-term stability. Compared with previously reported capacitive pressure sensors, the proposed device shows a wide sensing range combined with competitive sensitivity (**Table S3**).

Mechanical Properties of Gradient Porous Pressure Sensors

To comprehensively evaluate the influence of the gradient porous structures on mechanical performance, we conducted quasi-static compression tests on four typical structures: TGPS-1 (Gradient), TGPS-6 (Larg-pore), TGPS-7 (Medium-pore), and TGPS-8 (Small-pore). The corresponding compressive stress–strain curves are shown in **Fig. 3h**. Dielectric layers with larger pore structures exhibit higher compressibility and elasticity, with a low compressive stress of only 15 kPa at 30% strain. This behavior is attributed to the higher porosity of large-pore structures, which renders them more prone to bending deformation and confers a lower elastic modulus. In contrast, dielectric layer with smaller pore structure possesses higher bending strength due to their denser pores, resulting in greater mechanical strength and robustness, with a high compressive stress of 473 kPa at 60% strain. As shown in **Fig. 3i**, at a low compressive strain of 5%, the compressive modulus follows the order: small-pores > medium-pores > gradient > large-pores. Notably, the compressive modulus of the gradient structure is closer to the average of the medium- and large-pore sizes. However, when the strain increases to 50%, the order shifts to: small-pores > gradient > medium-pores > large-pores, with the gradient structure's modulus now approaching the average of the medium- and small-pore sizes. This transition arises from the unique hierarchical

compression mechanism of the gradient porous architecture. At low strains, the large-pore layer, possessing the highest compressibility, deforms first and dominates the overall mechanical response, resulting in an initial modulus closer to that of the large-pore structure and lower than that of the medium-pore sample. As strain increases, the medium- and small-pore layers progressively engage in load bearing, significantly elevating the overall structural stiffness. This design effectively combines the high compressibility of large pores with the strong mechanical robustness of smaller pores. Under dynamic loading, hysteresis is a key factor affecting sensor stability. **Fig. 3j** presents the hysteresis behavior of the sensor at different strain levels. Even after large deformation up to 80% strain, the sensor can almost fully recover to its original state, demonstrating excellent elastic recovery and high structural reversibility of the gradient porous design.

Wearable Pressure Sensing Devices

The proposed sensors show significant potential in health monitoring and human joint motion detection. As shown in **Fig. 4a–e**, the sensor was attached to the finger, wrist, elbow, knee joints and throat. When the finger bends from 30° to 90°, the sensorxhibits a clear capacitive response, with the capacitance variation increasing proportionally with bending angle, confirming high sensitivity and fast response. Cardiovascular disease remains a leading cause of death and disability worldwide. Tactile sensing of physiological signals plays an important role for early prevention, as it reflects circulatory and respiratory function. Our sensors can detect subtle arterial pulse signals from the radial and carotid arteries. Attached to the radial artery of a 24-year-old healthy volunteer, the sensor acquired real-time pulse signals (**Fig. 4f**). Fast Fourier transform (FFT) analysis (**Fig. 4g**) reveals a dominant frequency of 1.15 Hz, corresponding to $\approx$ 69 bmp. Similarly, carotid artery measurement (**Fig. 4h**) presents a dominant frequency of 1.10 Hz (~60 bpm) (**Fig. 4i**), both within the normal adult range. Importantly, the sensor clearly distingwishs the three characteristic peaks of the arterial pulse waveform, the percussion wave (P wave), tidal wave (T wave), and diastolic peak (D wave), which

is consistent with clinical standards. These results demonstrate the excellent performance of our flexible sensor in both physiological signal detection and joint motion sensing, making it suitable for diverse wearable applications.

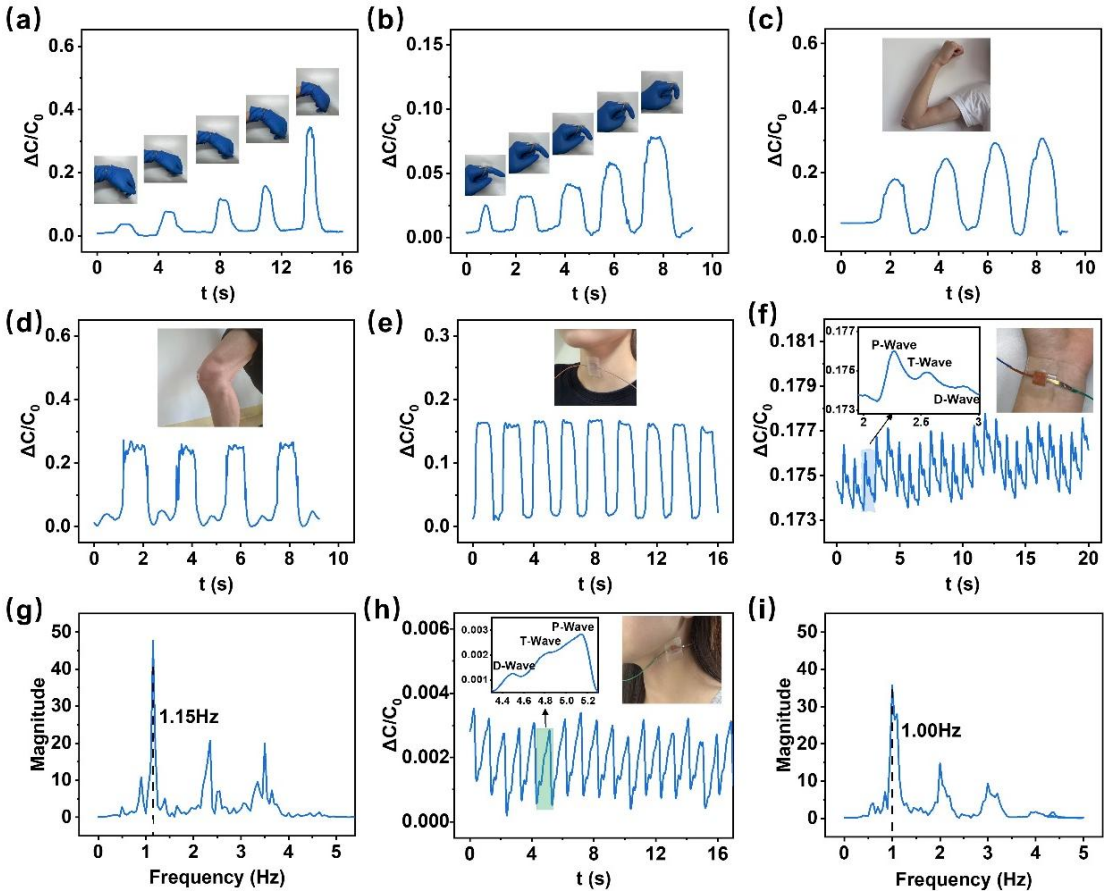


Fig. 4 Demonstration of the capacitive pressure sensor for detecting various external stimuli. **a-e** Relative capacitance changes upon bending of the wrist (a), finger (b), elbow (c), and knee (d), as well as swallowing (e). **f** Real-time radial pulse signal from the wrist. **g** Fast Fourier transform of the radial pulse to assess the pulse rate. **h** Real-time carotid pulse signal from the neck. **i** Fast Fourier transform of the carotid pulse signal to assess the pulse rate.

Flexible Pressure Sensor Combined with Machine Learning for Speech Recognition.

Millions of people worldwide suffer from speak disorders caused laryngeal resection, vocal cord paralysis, or other voice-related conditions. Neck muscle activity is closely

correlated with the articulation of different spoken words. In this work, we employ a flexible pressure sensor to capture subtle signals generated by neck muscle movements during speech, and apply machine learning algorithms for signal classification and speech recognition (**Supporting Project Documents 4**).

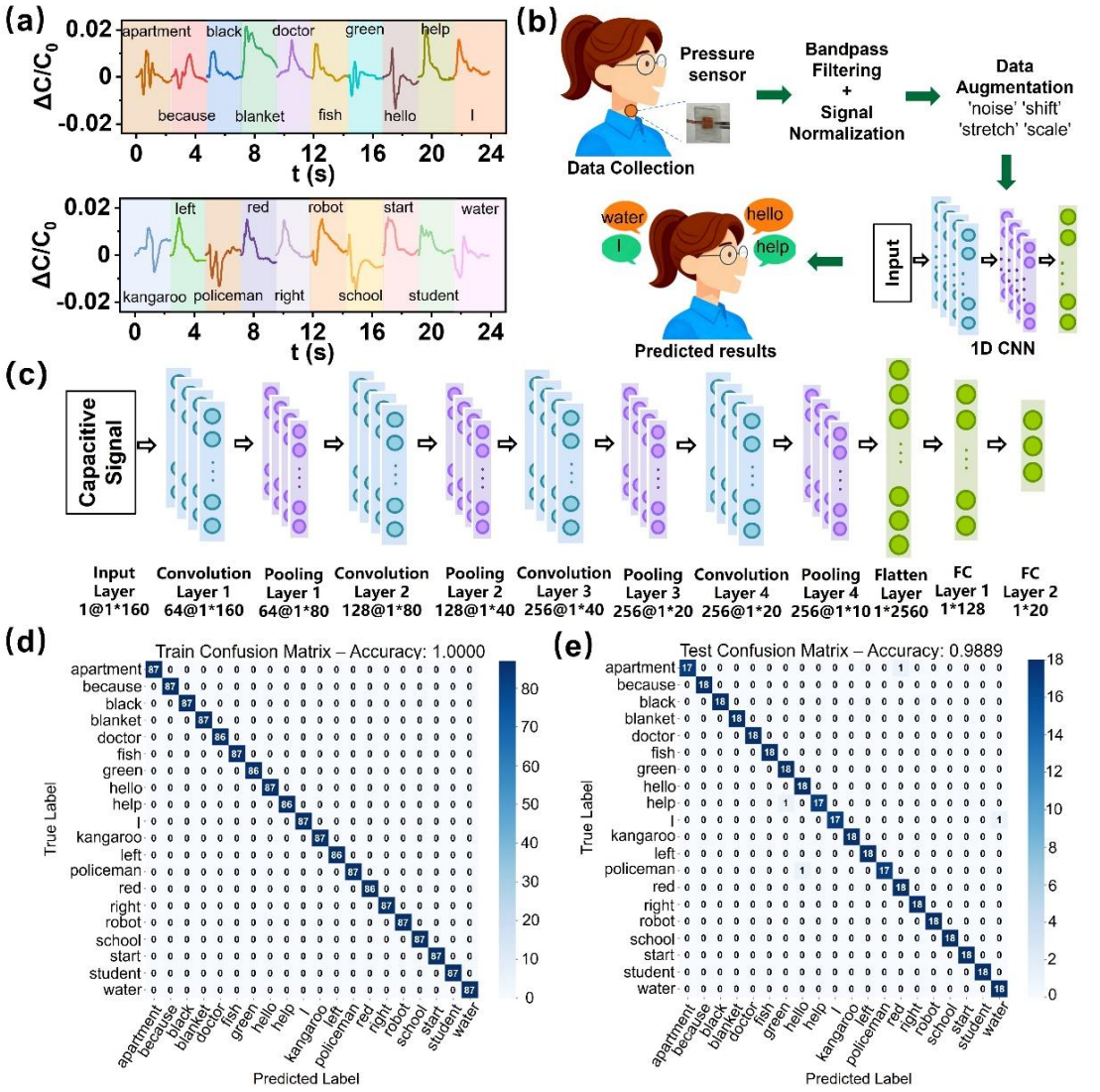


Fig. 5 Speech recognition based on flexible pressure sensors and machine learning. **a** Response waveforms of the sensors for seven categories of words (including 20 words such as “apartment,” “because,” “I,” “help,” and “hello”). **b** Flowchart of the speech recognition process. **c** Schematic diagram of the speech recognition convolutional neural network algorithm. **d** Confusion matrix of speech prediction results against the training dataset. **e** Confusion matrix of speech prediction results versus the test dataset.

To evaluate the speech recognition capability, the flexible pressure sensor was used to collect neck muscle motion signals from volunteers while they spoke 20 common words. **Fig. 5a** shows the characteristic capacitance variation waveforms induced by laryngeal muscle vibrations for each word. The vocabulary include "apartment," "because," "I," "help," "hello," etc., covering different syllables and pronunciation patterns. Most words exhibit distinct signal features, although some show partially similar patterns. Each word was repeated 30 times under natural speaking conditions. Machine learning algorithms were subsequently employed to classify these signals. **Fig. 5b** illustrates the overall speech recognition workflow, encompassing data acquisition and preprocessing, including filtering and signal normalization. To address the limited dataset size and improve model generalization, data augmentation was used to automatically generate three augmented versions of each original sample. Specifically, Gaussian noise was added to simulate environmental interference, time shifting was used to account for variations in speaking rhythm, time stretching was applied to cover different speaking speeds, and amplitude scaling was introduced to improve robustness against variations in speech intensity. This augmentation strategy effectively expanded the total dataset from 600 samples to 2,400 samples.

For machine learning, 70% of the dataset was randomly selected for training, 15% for validation, and 15% for testing. **Fig. 5c** shows the designed one-dimensional convolutional neural network (1D-CNN), which automatically extracts temporal features through multiple convolutional layers. Batch normalization, ReLU activation, max pooling, and dropout layers were incorporated to improve feature representation and reduce overfitting. A fully connected layer was finally used for multi-class classification. During training, the model was optimized using the cross-entropy loss function and the Adam optimizer. After each epoch, model performance was evaluated using the validation set. When the validation loss decreases, the current model was saved as the best model. Otherwise, a patience counter is increased. If the validation loss fails to improve over several consecutive iterations, an early stopping strategy was employed to terminate training and prevent model overfitting. The detailed workflow

is shown in **Fig. S8**. Finally, the recognition accuracy reached 100% on the training set (**Fig. 5d**) and 98.89% on the test set (**Fig. 5e**). These results demonstrate that the machine learning-assisted flexible pressure sensor is feasible for detecting laryngeal muscle movements and performing speech recognition, showing strong potential for healthcare applications and human–machine interaction.

Conclusions

In summary, we have proposed a method that combines machine learning with finite element simulation for the rational design of gradient porous structures in flexible pressure sensors. Fabricated via a simple sacrificial template method, the optimized sensors exhibit high sensitivity (0.02 kPa^{-1}), a wide pressure detection range (0–600 kPa), fast response times (75ms), and excellent stability. Owing to these outstanding performance characteristics, the sensor successfully monitors arterial pulse signals and joint bending motions at the fingers, wrist, elbow, and knee. Furthermore, when integrated with machine learning, the sensor achieves 98.89% accuracy in a 20-word speech recognizing task, demonstrating its potential for assisting patients with voice loss caused by laryngeal diseases. These results position the sensor as a promising candidate for applications in motion monitoring, electronic skin, and next-generation wearable sensing systems.

Experimental section

Fabrication of the TGP dielectric layer: Figure S1 shows the fabrication process of the TGP dielectric layer. PMMA particles with different sizes were used as sacrificial templates. Small-sized PMMA particles, PDMS prepolymer, and curing agent (Sylgard 184, Dow Corning, USA) were thoroughly mixed at a mass ratio of 10:8:1. The mixture was mechanically stirred and then degassed under vacuum (0.08 MPa, 10 min) to obtain a uniformly dispersed composite slurry. The slurry was then coated onto a pre-fabricated mold using spin-coating or blade-coating to form the first layer. After curing at 60 °C for 30 min in an oven, a second mixture containing medium-sized PMMA

particles, PDMS prepolymer, and curing agent (10:8:1 by mass ratio) was poured onto the first layer and cured at 60 °C for 30 min to form the second layer. Subsequently, a third mixture containing large-sized PMMA particles, PDMS prepolymer, and curing agent (10:8:1 by mass ratio) was added on top of the second layer and cured again at 60 °C for 30 min, resulting in a fully cured three-layer structure with a gradient architecture. The obtained structure was then repeatedly immersed in ethyl acetate (E116132, Aladdin, China) solution to remove the sacrificial PMMA templates. Finally, the sample was soaked in ethanol to eliminate residual ethyl acetate and naturally dried at room temperature, yielding the three-layer gradient porous (TGP) dielectric layer.

Fabrication of the capacitive pressure sensor: The TGP dielectric layer was cut into a size of 10 mm × 10 mm. The size and thickness of the TGP dielectric layer are shown in F**igure S2a**. As shown in **Figure S2b**, the fabricated dielectric layer exhibits good flexibility and can be bent or twisted into arbitrary shapes. To ensure strong adhesion between the electrodes and the dielectric layer, printed electrode sheets were coated with conductive silver paste and placed on both sides of the dielectric layer, followed by thermal curing at 80 °C on a hot plate for 1 h. Finally, the device was encapsulated with polyimide (PI) tape, and the capacitive pressure sensor based on the TGP structure was successfully fabricated.

Material Characterization: A scanning electron microscope (Regulus 8230, HITACH, Japan) was used to characterize the morphology of the dielectric layer. An experimental setup consisting of a mechanical testing machine (QX-W100, Shanghai Qixiang Detection Equipment Co. Ltd, China), a custom-built capacitive signal acquisition circuit board, and a personal computer was used to characterize the capacitive response of the pressure sensor (**Fig. S3**).

Design of the capacitive signal acquisition circuit board: All capacitive signals were acquired using the custom-built capacitive signal acquisition circuit board. **Fig. S4** shows a block diagram of the data acquisition system. The schematic diagram and PCB layout of the capacitive signal acquisition circuit board are shown in **Fig. S5**. To address the susceptibility of capacitive signals to external interference, two independent

single-core shielded wires were employed, each consisting of a signal line and an independent braided shield. The signal lines were connected to the two electrodes of the sensor and the differential input ports of the FDC2114, respectively. The shielding layers of both cables are grounded, while the sensor ends are left floating (**Fig. S6**). The grounded shielding layers form a continuous Faraday cage surrounding the signal lines, which efficiently captures external electromagnetic fields and directs them to the system's reference ground, preventing them from coupling to the signal lines. Furthermore, this converts the unstable parasitic capacitance between the signal lines and ground into a relatively fixed parasitic capacitance relative to ground. The converted capacitance becomes a DC offset that can be calibrated by the system, thereby significantly suppressing signal drift caused by cable movement or human proximity.

Finite Element Simulation: Performed using COMSOL Multiphysics software. The model was constructed using the actual dimensions of the gradient porous dielectric layer. The material of the dielectric layer was set to the hyperelastic Mooney-Rivlin model.

Acknowledgements

This work was supported by the National Natural Science Foundation of China (T2225026, 52202344, 82172087), the Beijing Natural Science Foundation (25B10448), and the National Key R&D Program of China (2022YFA1205801).

Data Availability Statement

The data that support the findings of this study are available from the corresponding author upon reasonable request.

References

1. Mohamadzade, S., Safavi-Mirmahalleh, S. A., Habibzadeh, S., Behboodi-Sadabad, F., & Salami-Kalajahi, M. (2025). A review on application of nanomaterials in flexible pressure sensors. *Materials Today Nano*, *30*, 100627.

10.1016/j.mtnano.2025.100627

2. Duan, M., Dang, X., Chen, X., He, H., Tian, X., Chen, M., ... & Wang, Q. (2025). Dual-mechanism relay capacitive pressure sensors with ultra-wide linear range and high sensitivity based on 3D periodic lattice elastomer integrated with ionic gel. *Chemical Engineering Journal*, *519*, 165296.

10.1016/j.cej.2025.165296

3. Liu, L., Mo, L., Han, S., Liu, X., Sun, J., Han, Z., ... & Li, H. (2026). Enhancing Flexible Capacitive Sensor Performance through the Synergy of Thermally Expandable Microspheres and Carbon Nanotubes via 3D Direct Ink Writing. *Advanced Functional Materials*, *36*(9), e14093.

https://doi.org/10.1002/adfm.202514093

4. Cheng, J., Lei, Q., Yang, Q., Chen, L., Lou, D., Tao, Q., ... & Liu, D. (2025). Sequentially squeezed capacitive pressure sensor based on baguette-inspired porous ionic gel foams. *Chemical Engineering Journal*, 171362.

10.1016/j.cej.2025.171362

5. Li, A., Xu, J., Xu, D., Zhang, Z., Cao, D., Li, J., ... & Zhang, F. (2025). High-performance, breathable, and degradable fully cellulose-based sensor for multifunctional human activity monitoring. *Chemical Engineering Journal*, *505*, 159564.

10.1016/j.cej.2025.159564

6. Chen, M., An, X., Zhao, F., Chen, P., Wang, J., Zhang, M., & Lu, A. (2025). Boosting sensitivity of cellulose pressure sensor via hierarchically porous structure. *Nano-Micro Letters*, *17*(1), 205.

https://doi.org/10.1007/s40820-025-01718-z

7. Ren, L., Li, Y., Wang, Y., Zhang, X., & Qiang, T. (2025). MXene/polyurethane

flexible films for wearable pressure sensors with high sensitivity and electromagnetic shielding. *ACS Applied Polymer Materials*, *7*(10), 6393-6402.
https://doi.org/10.1021/acsapm.5c00830
8. Chen, H., Mao, Z., Zhang, T., Xu, X., & Qiang, X. (2025). Conductive polyurethane sponge modified with Gr/EC nanocomposite for high-performance pressure sensor. *Surfaces and Interfaces*, 107698.
10.1016/j.surfin.2025.107698
9. Ma, J., Lu, Y., Li, J., Rong, Z., Wei, A., & Liu, Z. (2025). Flexible pressure sensors based on electrospun PAN fiber films incorporated with graphene/polypyrrole composites and engineered PDMS microstructures. *Journal of Materials Chemistry A*, *13*(28), 22695-22709.
https://doi.org/10.1039/D5TA01873K
10. Chun, B., Park, J., Bang, J., Lim, J., Han, Y., & So, H. (2025). Polypyrrole/Polydimethylsiloxane Sponge-Based Flexible Pressure Sensors with Enhanced Sensitivity and a Wide Detection Range Using Programmable Gradient Pore Density. *ACS Applied Electronic Materials*, *7*(13), 6002-6014.
https://doi.org/10.1021/acsaelm.5c00654
11. Tang, X., Yang, J., Luo, J., Cheng, G., Sun, B., Zhou, Z., ... & Wei, D. (2024). A graphene flexible pressure sensor based on a fabric-like groove structure for high-resolution tactile imaging. *Chemical Engineering Journal*, *495*, 153281.
10.1016/j.cej.2024.153281
12. Wang, M., Wang, G., Zheng, M., Liu, W., Lv, W., Ma, Y., ... & Ebo, B. (2025). High-performance flexible pressure sensor based on synergistic enhancement of magnetic field oriented carbon Nanotube/Graphene and microdome array structure. *Chemical Engineering Journal*, *511*, 162053.
10.1016/j.cej.2025.162053
13. Xu, R., Cao, P., Zhang, T., Wei, J., Wang, Y., Huang, Z., ... & Chen, Y. (2026). Biomimetic Multiscale-Structured Biomass Graphene/Polyurethane Sponge Composite for Flexible Pressure Sensors and Intelligent Cushioning Materials. *Advanced*

Science, *13*(8), e17511.
https://doi.org/10.1002/advs.202517511
14. Zhang, J., Zhang, X., An, X., Chen, J., Wang, S., Wang, X., ... & Li, L. (2025). Forward Design of Single Ultra-Wide Range and Highly Sensitive Flexible Pressure Sensor for Multi-Physiological-Motion Monitoring. *Advanced Healthcare Materials*, *14*(31), e01798.
https://doi.org/10.1002/adhm.202501798
15. Zhang, H., Yang, C., Xia, H., An, W., Qi, M., & Zhang, D. (2025). Layer-by-layer self-assembled honeycomb structure flexible pressure sensor array for gait analysis and motion posture recognition with the assistance of the ResNet-50 neural network. *ACS sensors*, *10*(3), 2358-2366.
https://doi.org/10.1021/acssensors.5c00187
16. Peng, W., Zhu, R., Zhu, X., Zhang, C., & Liao, L. (2026). Flexible arrayed triboelectric pressure sensor with PDMS/CNT/CB variable-curvature friction layer for robotic tactile sensing. *Nano Energy*, 111829.
10.1016/j.nanoen.2026.111829
17. Habib, A., Sapuan, S. M., Zainudin, E. S., & Atiqah, A. (2025). A flexible pressure sensor based on arrowroot starch/CNT bio-nanocomposite films for piezoelectric application. *Biomass and Bioenergy*, *202*, 108243.
10.1016/j.biombioe.2025.108243
18. Alidoust, A., Haghgoo, M., Ansari, R., Hassanzadeh-Aghdam, M. K., & Jang, S. H. (2025). A mapped conductive network model on the simulation of aligned CNT/PDMS flexible pressure sensor piezoresistivity. *Composites Part A: Applied Science and Manufacturing*, *191*, 108750.
https://doi.org/10.1016/j.compositesa.2025.108750
19. Oyunbaatar, N. E., Wei, J., Wang, L., Kim, S. H., Lee, H., Kwon, K., ... & Lee, D. W. (2025). 3D-printed CNT-reinforced bioresorbable vascular scaffold with enhanced mechanical stability and integrated wireless pressure sensor for continuous hemodynamic monitoring. *ACS sensors*, *10*(8), 5724-5735.

https://doi.org/10.1021/acssensors.5c00857

20. Jiang, Y., Zhao, C., Song, Z., Jia, R., Liu, J., Liu, X., ... & Zhang, C. (2026). MXene-Triggered 3D Printing of Gradient-Modulus Iontronic Pressure Sensors for Adaptive Robotic Grasping. *Advanced Functional Materials*, *36*(24), e22891.

https://doi.org/10.1002/adfm.202522891

21. Zhou, A., Wu, Z., Bai, Q., Zhang, X., Li, X., Shen, H., ... & Liu, S. (2026). MXene-thermochromic hybrid films for interference-free dual-mode sensing in wearable healthcare. *Advanced Functional Materials*, *36*(15), e22165.

https://doi.org/10.1002/adfm.202522165

22. Cheng, Y., Wang, M., Ma, N., Zhang, R., Cai, Z., Liu, M., ... & Li, L. (2025). Nanoscale Interlayer Engineering Enhances MXene-Based Flexible Pressure Sensor. *Nano Letters*, *25*(31), 11782-11789.

https://doi.org/10.1021/acs.nanolett.5c01464

23. Chen, J., Song, T., Wang, X., Zhou, Y., Wang, T., Zhang, X., ... & Han, W. (2024). Ultrasensitive and wide-range MXene/PDMS piezoresistive sensors inspired by rose petals. *Nano Energy*, *131*, 110285.

10.1016/j.nanoen.2024.110285

24. Jin, Y., Shen, H., Sun, L., Zhou, X., & Chen, L. (2024). Multilevel nanostructured pressure sensor for object recognition with Deep-Learning assistance: A strategy for high sensitivity and wide detection range. *Chemical Engineering Journal*, *484*, 149298.

10.1016/j.cej.2024.149298

25. Zhao, W., Li, K., Li, Z., Wang, W., Yu, X., Zhang, T., & Yang, X. (2025). Flexible pressure sensor arrays with high sensitivity and high density based on spinous microstructures for carved patterns recognition. *Advanced Functional Materials*, *35*(11), 2417238.

https://doi.org/10.1002/adfm.202417238

26. Han, S., Liu, C., Huang, Z., Zheng, J., Xu, H., Chu, S., ... & Liu, C. (2019). High-performance pressure sensors based on 3D microstructure fabricated by a facile transfer

technology. *Advanced Materials Technologies*, *4*(5), 1800640.
https://doi.org/10.1002/admt.201800640

27. Yang, S., Kim, S., & Kim, J. (2025). A Graphene/Ecoflex Reinforced Fabric (GERF) Capacitive Pressure Sensor by Increasing Dielectric and Mechanical Properties for Wide Sensing Range. *Fibers and Polymers*, *26*(4), 1803-1814.
https://doi.org/10.1007/s12221-025-00883-7

28. Zhong, Y., Liu, Y., Song, J., Hu, M., Cheng, G., & Ding, J. (2025). A high-performance flexible self-powered pressure sensor based on Co-MOF/Ecoflex and PVDF/Ecoflex double triboelectric layer. *Journal of Alloys and Compounds*, 183268.
https://doi.org/10.1016/j.jallcom.2025.183268

29. Chen, R., Luo, T., Wang, J., Wang, R., Zhang, C., Xie, Y., ... & Zhou, W. (2023). Nonlinearity synergy: An elegant strategy for realizing high-sensitivity and wide-linear-range pressure sensing. *Nature Communications*, *14*(1), 6641.
https://doi.org/10.1038/s41467-023-42361-9

30. Song, Y., Ren, W., Zhang, Y., Liu, Q., Peng, Z., Wu, X., & Wang, Z. (2023). Synergetic Monitoring of both Physiological Pressure and Epidermal Biopotential Based on a Simplified on-Skin-Printed Sensor Modality. *Small*, *19*(45), 2303301.
https://doi.org/10.1002/smll.202303301

31. Chen, X., Luo, Y., Chen, Y., Li, S., Deng, S., Wang, B., ... & Shao, J. (2024). Biomimetic contact behavior inspired tactile sensing array with programmable microdomes pattern by scalable and consistent fabrication. *Advanced Science*, *11*(43), 2408082.
https://doi.org/10.1002/advs.202408082

32. Tu, S., Xi, Y., Cui, X., Xu, Z., Liu, Z., & Zhu, Y. (2024). Skin-inspired interlocked microstructures with soft-hard synergistic effect for high-sensitivity and wide-linear-range pressure sensing. *Chemical Engineering Journal*, *496*, 154083.
10.1016/j.cej.2024.154083

33. Zhang, Z., Zhang, Q., Zhang, H., Li, B., Zang, J., Zhao, X., ... & Xue, C. (2023). A novel MXene-based high-performance flexible pressure sensor for detection of human

motion. *Smart Materials and Structures*, *32*(6), 065007.
10.1088/1361-665X/accee9
34. Wang, S., Deng, W., Yang, T., Ao, Y., Zhang, H., Tian, G., ... & Yang, W. (2023). Bioinspired MXene-based piezoresistive sensor with two-stage enhancement for motion capture. *Advanced functional materials*, *33*(18), 2214503.
https://doi.org/10.1002/adfm.202214503
35. Lu, P., Xu, J., Wang, X., Lian, W., Li, C., & Guan, S. (2024). Gradient pore structured Ppy/PDMS conductive sponge for flexible pressure sensor. *Chemical Engineering Journal*, *488*, 151049.
10.1016/j.cej.2024.151049
36. Zhang, X., Sun, K., Ma, J., Lin, K., Chen, Z., Zhu, G., ... & Xu, J. (2025). Gradient Porous Flexible Pressure Sensors with the Relay Effect for High-Accuracy Braille-to-Speech Recognition. *ACS sensors*, *10*(9), 7035-7050.
https://doi.org/10.1021/acssensors.5c02096
37. Jin, Y., Xue, S. A., & He, Y. (2025). Flexible Pressure Sensors Enhanced by 3D-Printed Microstructures. *Advanced Materials*, *37*(27), 2500076.
https://doi.org/10.1002/adma.202500076
38. Luo, Y., Abidian, M. R., Ahn, J. H., Akinwande, D., Andrews, A. M., Antonietti, M., ... & Chen, X. (2023). Technology roadmap for flexible sensors. *ACS nano*, *17*(6), 5211-5295.
https://doi.org/10.1021/acsnano.2c12606
39. Wang, B., Kong, D., He, Z., Liang, J., Lu, Y., Deng, Z., ... & Yang, G. (2026). Customizing Tactile Sensors via Machine Learning-Driven Inverse Design. *Advanced Science*, e24250.
https://doi.org/10.1002/advs.202524250
40. Ma, C., Li, G., Qin, L., Huang, W., Zhang, H., Liu, W., ... & Li, S. T. (2021). Analytical model of micropyramidal capacitive pressure sensors and machine-learning-assisted design. *Advanced Materials Technologies*, *6*(12), 2100634.
https://doi.org/10.1002/admt.202100634

Supplementary Files

This is a list of supplementary files associated with this preprint. Click to download.

- SI.docx